

Strain-induced local surface chemical ordering observed by STM

G. Ritz, M. Schmid, A. Biedermann, and P. Varga

Institut für Allgemeine Physik, Technische Universität Wien, A-1040 Wien, Austria

(Received 26 September 1995; revised manuscript received 9 February 1996)

PtNi alloys are known to exhibit a tendency towards chemical ordering, which also effects surface segregation. Scanning tunneling microscopy results obtained in the strain field of dislocations on $\text{Pt}_x\text{Ni}_{1-x}$ (110) surfaces show a (2×1) superstructure of alternating Pt and Ni atoms in some regions close to the dislocation core. In other regions, the apparent height of all surface atoms is equal, in agreement with low energy ion scattering results yielding a surface concentration of almost 100% Ni. This indicates that the strain present in the vicinity of dislocations influences both the surface composition and chemical order. The experimental results are compared to simulation calculations of chemical ordering and segregation, using embedded atom method potentials and linear elasticity theory. The simulations indicate that the (2×1) superstructure is due to an $L1_0$ ordered phase in regions where the tetragonal distortion of the $L1_0$ phase with respect to the cubic substrate can alleviate stress. It is argued that this dislocation-induced ordering can immobilize dislocations. [S0163-1829(96)03624-7]

I. INTRODUCTION

The Pt–Ni alloy system is very interesting, both from the technological and the physical point of view. On the one hand, there are industrial applications in heterogenic catalysis. On the other hand, the PtNi system exhibits several unusual features. It has been found that surface segregation leads to an oscillating depth profile and that it depends on the surface orientation which constituent segregates.^{1–3} For the (100) and the (111) surfaces, the topmost layer is enriched with Pt, whereas the (110) surface consists of almost pure Ni.^{4,5} The PtNi alloys have also a strong tendency to form ordered structures ($L1_2$ at a Pt concentration of 25% with critical temperature of 853 K and $L1_0$ at a Pt concentration of 50% with critical temperature of 918 K), which leads to short range chemical ordering.⁶

Preferential sputtering of the Ni during sample preparation is known to lead to a Pt enriched altered layer with a thickness of approximately 1 nm – 1.5 nm corresponding to ≈ 10 monolayers on (110).^{7–9} Subsequent annealing at temperatures below 870 K yields segregation of Pt within the altered layer, which causes a higher Pt concentration in the topmost layers then it would be in the true thermodynamic equilibrium.^{9,10} The Pt enrichment leads to misfit dislocations, due to the increased lattice constant in the altered layer. Only at annealing temperatures above 870 K does the bulk diffusion become effective and the altered layer gradually disappears.

In this paper, we present another interesting segregation phenomenon found on the PtNi (110) surface. Scanning tunneling microscopy (STM) experiments have shown a (2×1) corrugation superstructure in the strain field of dislocations on $\text{Pt}_{10}\text{Ni}_{90}$ and $\text{Pt}_{25}\text{Ni}_{75}$ (110) surfaces, whereas atoms in other regions have the same apparent height. As will be shown this superstructure is due to chains of alternating Pt and Ni atoms, i.e., local Pt enrichment of the surface in the strained regions. The experimental results will be compared to embedded-atom method (EAM) computer simulations and calculations based on linear elasticity theory. Fi-

nally, a simple model explaining the driving force for the chemical ordering will be presented, which shows that the changed segregation behavior is not due to a metastable phase becoming energetically favored, as could be derived from theoretical predictions.^{11,12}

II. STM RESULTS

A. Experiment

All STM work was done with a modified commercial instrument (Omicron micro-STM) in an UHV system, consisting of a preparation chamber connected to the STM chamber. The samples have been cleaned by repeated cycles of sputtering (500 eV Ar^+) at an angle of 46° to the surface and annealing to temperatures of 670 K – 770 K by electron bombardment of the sample holder. The surfaces have been routinely checked by Auger electron spectroscopy and no contaminations have been found. Two different PtNi alloy single crystals with (110) surface orientation have been investigated: one with 10% platinum in the bulk and the other with 25% Pt. Due to preferential sputtering of Ni, approximately the first ten layers are Pt enriched.^{7,9}

B. Sputterinduced edge dislocations and screw dislocations on $\text{Pt}_x\text{Ni}_{1-x}$ (110) surfaces

As mentioned before, the undisturbed (110) surface of $\text{Pt}_x\text{Ni}_{1-x}$ alloys (with $x=0.1$ and $x=0.25$) are known to be almost pure Ni, due to surface segregation.^{4,5} However, in a real surface, there are several kinds of defects present. Two kinds of defects have been investigated in this work.

On the one hand, there are screw dislocations reaching the surface. These defects are bulk defects reaching the surface.

On the other hand, there are subsurface edge dislocations, due to surface Pt enrichment, which is caused by preferential sputtering of Ni. Because Pt has a larger lattice constant than Ni (11%), the surface layers do not fit on the substrate yielding mismatch dislocations.⁹ These subsurface dislocations can be seen in the STM as “ditches.” At the ends of these

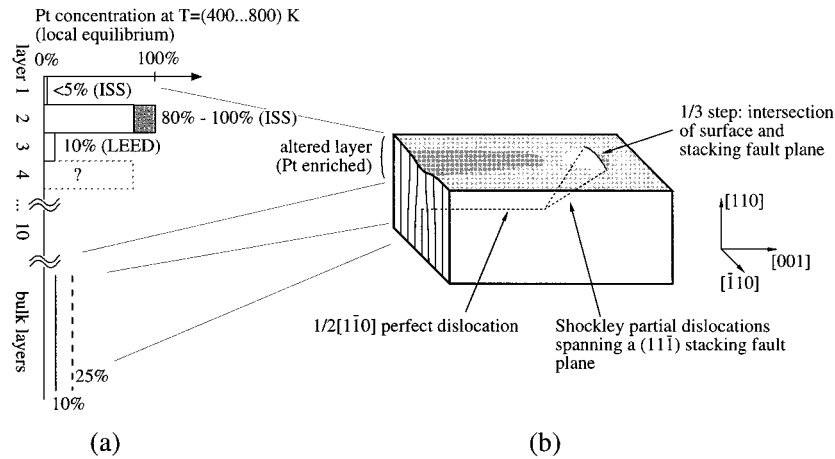


FIG. 1. (a) Compositional profile of the first three atomic layers in the Pt enriched altered layer of a PtNi (110) surface, determined by ISS (Refs. 4 and 5) and LEED (Ref. 13). The Pt enrichment is caused by preferential sputtering of Ni and Pt segregation within the altered layer during sample preparation. The composition is only a local equilibrium within the altered layer, as bulk diffusion is not effective at temperatures below 870 K (Refs. 9 and 10). (b) Schematic view of a mismatch dislocation below the (110) surface. The Pt enriched altered layer has a larger lattice constant and therefore does not fit on the substrate, which causes perfect $1/2[1\bar{1}0]$ dislocations. At their ends, the dislocations split into partials spanning a $(11\bar{1})$ stacking fault plane, which intersects the surface in a $1/3$ step (Ref. 9).

ditches, the dislocations reach the surface and one can determine their Burgers vector. A schematic view of the altered layer with a misfit dislocation is shown in Fig. 1, together with the Pt concentration of the first layers determined by ion scattering spectroscopy^{4,5} and low energy electron diffraction.¹³ The compositional depth profile with alternating layers consisting of mainly Ni and Pt indicates some kind of order in the altered layer. The lattice constant and, therefore, the density of the misfit dislocations depends on the composition of the altered layer.⁷⁻⁹

Figure 2 shows a STM image of the $\text{Pt}_{10}\text{Ni}_{90}(110)$ surface. There are several ends of short sputter-induced edge dislocations visible. In this area, one can easily see the pattern of alternating brighter and darker atoms giving a (2×1) superstructure whereas, in undisturbed regions, all atoms have approximately the same brightness.

Due to the subsurface edge dislocation, there is one row of atoms missing above the dislocation core. Therefore, the surface is obviously expanded in this region in $[\bar{1}10]$ direction (along the close packed rows). For a complete analysis,

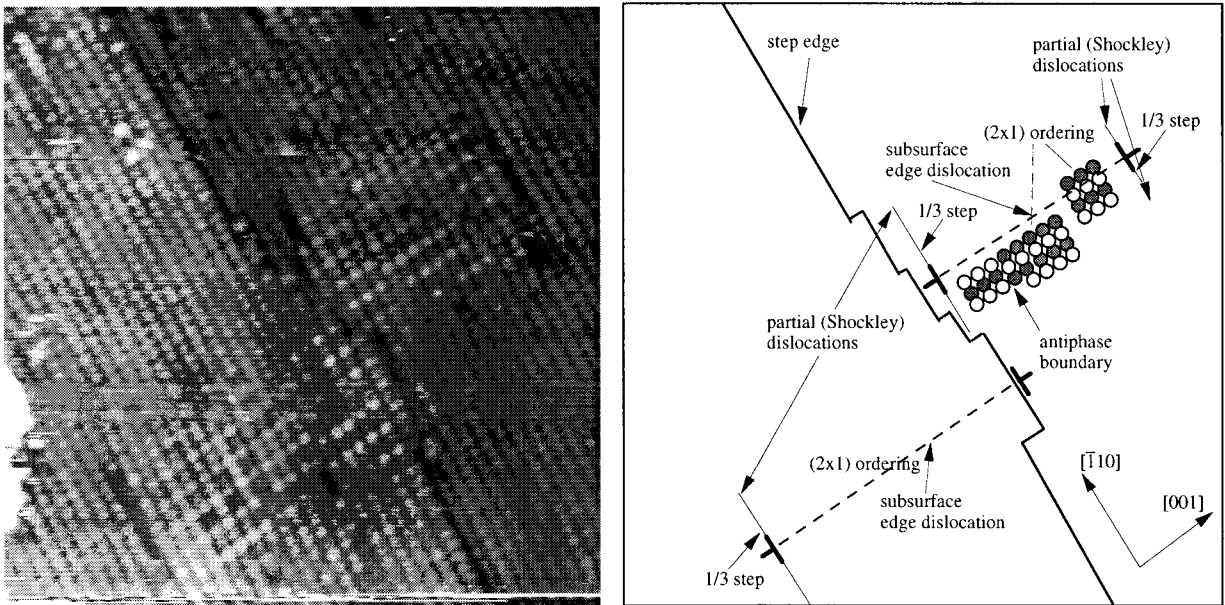


FIG. 2. Left part: $15 \text{ nm} \times 15 \text{ nm}$ STM image (contrast enhanced) of the $\text{Pt}_{10}\text{Ni}_{90}(110)$ surface, right part: schematic drawing of the features in the STM image. A (2×1) superstructure is visible above two subsurface edge dislocations. At the ends of the dislocation lines, the perfect dislocations split into two Shockley partials forming (111) or $(1\bar{1}\bar{1})$ stacking fault planes, with $\frac{1}{3}$ steps between them (Ref. 9). An antiphase boundary is also present where the ordering changes from bright-dark-bright to dark-bright-dark within only one lattice constant.

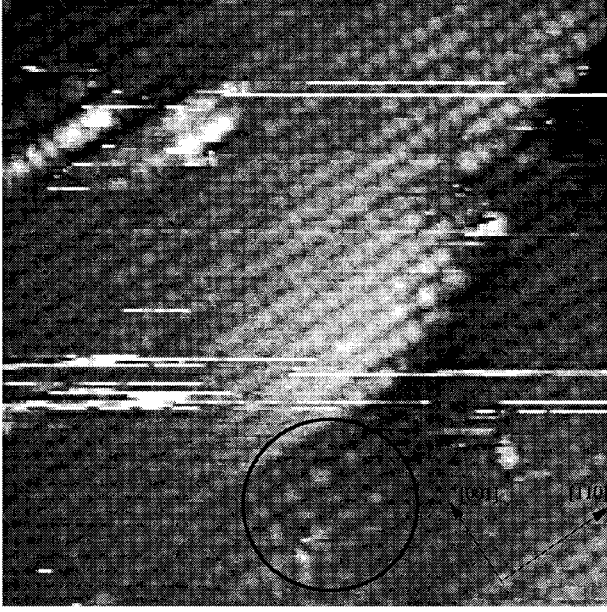


FIG. 3. 10 nm \times 10 nm STM image (contrast enhanced) of the Pt₁₀Ni₉₀ (110) surface. In the strained region (indicated by a circle) of a screw dislocation (bulk dislocation), the (2 \times 1) corrugation superstructure is visible.

it is necessary to know the exact atomic distances in both the undisturbed and the distorted regions. We have determined the atomic positions by using an image processing program based on the maximum entropy theory.¹⁴ It was found that near the end of an edge dislocation, the surface is expanded in both the $[\bar{1}10]$ and the $[001]$ direction. The estimated expansion is $\approx 5\%$ along the close packed rows ($[\bar{1}10]$), but only 1%–2% perpendicular to them ($[001]$).

Inspecting longer subsurface misfit dislocations, one can see that the superstructure only occurs at their ends. In the middle, where the surface is only expanded in $[\bar{1}10]$ direction but not in $[001]$, no corrugation pattern is visible.

It has to be noted that on the Pt₁₀Ni₉₀(110) surface the (2 \times 1) superstructure at the ends of sputter-induced dislocations is well reproducible. This indicates that no special tip conditions are necessary to observe this phenomenon and that it is present near the ends of all sputter-induced dislocations of the type shown in Fig. 1.

The (2 \times 1) corrugation superstructure could also be observed in the vicinity of bulk dislocations as can be seen in Fig. 3. In the expanded region near the dislocation core there are alternating brighter and darker atoms. In other regions, no such contrast pattern can be found. Unfortunately, it is not possible to estimate the expansion, in this case, because the (2 \times 1) regions are too small.

The same corrugation superstructure could be found — but only occasionally — on a Pt₂₅Ni₇₅(110) crystal near the core of a bulk dislocation. However, it is not always possible to observe this superstructure in STM images of bulk dislocations, even if the sample is prepared exactly the same way. In fact, during one measuring session, we obtained images of screw dislocations with and without the superstructure. This could be due to different orientations of the Burgers vector and of the dislocation line.

We have considered several possible explanations for the (2 \times 1) superstructure. The atoms could sit in different heights, due to some kind of ordering in the second layer. However, for symmetry reasons, there is no possible configuration that could yield a (2 \times 1) superstructure in the first layer. Electronic waves (charge density waves) cannot be the cause, as there are domain boundaries between differently ordered regions (see Fig. 2). The only remaining possibility is the differently bright atoms being of different species. Therefore, we conclude that the corrugation superstructure is due to chemical resolution. To verify this assumption, we have performed computer simulations.

III. SIMULATION CALCULATIONS

A. Embedded-atom method

For the simulation calculations, we used the embedded-atom method,¹⁵ which is a convenient tool for simulating the behaviour of fcc metals. The total energy is calculated as a sum of the individual contributions of each atom in the ensemble. For each atom, the energy consists of two parts: first, the energy for embedding the atom in the homogeneous surrounding electron gas with the density ρ_h and second, the energy due to pair potentials. Usually the latter is assumed to be repulsive. However, this is not the case for the potentials proposed by Voter *et al.*,¹⁶ which were used for the calculations in this paper. The total energy can be written as

$$E_{\text{tot}} = \sum_i F_i(\rho_{h,i}) + \frac{1}{2} \sum_{i,j} \Phi_{ij}(R_{ij}). \quad (1)$$

The first part of Eq. (1) is the sum over the individual embedding energies F_i for each atom i , due to the electron density $\rho_{h,i}$ of the surrounding atoms. The second part is the sum over all pair interactions. The host density $\rho_{h,i}$ is approximated by the sum over the individual electron densities of the neighboring atoms ρ^a ,

$$\rho_{h,i} = \sum_{j \neq i} \rho_j^a(R_{ij}). \quad (2)$$

For both, the electron densities and the pair potentials, Voter *et al.* used analytical expressions,

TABLE I. Parameters for the functions $\rho^a(R)$ and $\Phi(R)$ in Eq. (3) obtained by the fitting procedure. Due to the embedding energy, the R_0 parameters are different from the equilibrium distances.

	A ($\text{\AA}^{-(\beta+3)}$)	β	γ (\AA^{-1})
ρ_{Ni}	1.347	6	4.53
ρ_{Pt}	0.217	10	5.25
	D (eV)	α (\AA^{-1})	R_0 (\AA)
$\Phi_{\text{Ni-Ni}}$	2.8307	2.3601	2.0993
$\Phi_{\text{Pt-Pt}}$	0.0340	1.8963	3.2566
$\Phi_{\text{Pt-Ni}}$	0.9008	2.1605	2.4630

TABLE II. Formation enthalpies ΔH_{PtNi_3} , $\Delta H_{\text{Pt}_3\text{Ni}}$, and ΔH_{PtNi} for the $L1_2$ and $L1_0$ phases of PtNi used as input for the fitting procedure and calculated with the EAM potentials in eV/atom.

	ΔH_{PtNi_3}	ΔH_{PtNi}	$\Delta H_{\text{Pt}_3\text{Ni}}$
Input for fitting ^a	-0.098	-0.116	-0.091
EAM (unrelaxed)	-0.160	-0.186	-0.107
EAM (relaxed)	-0.160	-0.213	-0.107

^aReference 25.

$$\Phi(R) = D(e^{-2\alpha(R-R_0)} - 2e^{-\alpha(R-R_0)}),$$

$$\rho^a(R) = AR^\beta(e^{-|\gamma|R} + 2^{3+\beta}e^{-2|\gamma|R}). \quad (3)$$

The parameters D , α , R_0 , A , β , and γ were determined by a fitting procedure and are listed in Table I. The embedding energy as a function of the electron density is adjusted, so that the total energy matches the universal expression for the energy as a function of the lattice constant proposed by Rose *et al.*¹⁷ Special care has been taken to assure that the fitted potentials correctly reproduce the ordered $L1_2$ and $L1_0$ phases by forcing the superlattice intrinsic stacking fault, the complex stacking fault, and the antiphase boundary energies to be positive. The formation enthalpies for the $L1_2$ and $L1_0$ phases used as input data for the fit are listed together with the values calculated with our potentials in Table II. As can be seen, the EAM potentials overestimate the ordering energies, but since we will only compare energies of different configurations of the same ordered structure, this poses no problem.

The potentials yield resonable values for the differences in surface energies per atom [e.g., $\gamma_{\text{Ni}} - \gamma_{\text{Pt}}(110) = -0.18$ eV/atom] and, therefore, describe the segregation behavior, including the reversal on the (110) surface very well, as can be seen from Table III, whereas it is too weak¹⁸ with the EAM potentials published by Foiles.¹⁹ However, the tetragonal distortion of the $L1_0$ structure turns out to be overestimated by the calculations. The c/a ratio is $3.30 \text{ \AA} / 4.00 \text{ \AA} = 0.825$, instead of the experimental value $3.58 \text{ \AA} / 3.82 \text{ \AA} = 0.937$.

B. Simulation of the strained region with EAM

For the simulation of the strained region near the dislocation cores, we used a very simplified model: a slab with periodic boundaries in both surface directions, which has been expanded (and compressed) in both the $[\bar{1}10]$ and the $[001]$ directions by varying amounts to simulate the strain

TABLE III. Calculated Pt concentration in the topmost four layers of PtNi at $T=800$ K in at. % [in rough agreement with experimental data (Ref. 26)].

	c_{bulk}	c_1	c_2	c_3	c_4
(100)	11	17	6	13	11
(110)	11	3	23	5	13
(111)	11	17	9	12	12

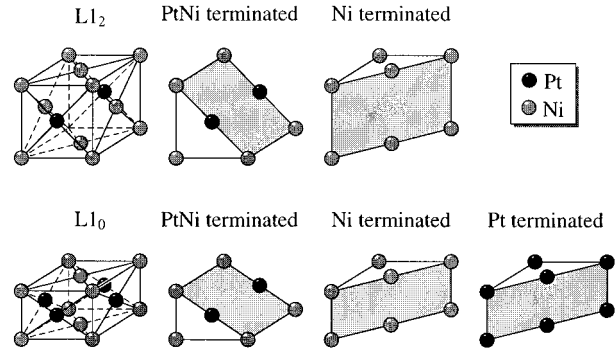


FIG. 4. The ordered $\{110\}$ surfaces of the $L1_2$ and $L1_0$ structures (truncated bulk structure). The tetragonal distortion of the $L1_0$ structure has been strongly exaggerated.

field of the dislocation. We, therefore, neglected any bending or shear of the surface in the distorted area.

The total energy of a given slab configuration is calculated by means of an energy minimization code, which uses a conjugate gradient algorithm for determination of atomic positions. Because compositional changes cannot be accounted for by this procedure, one has to compare the energies of different configurations to determine the energetically favored one.

Both ordered phases ($L1_2$ and $L1_0$) could cause the (2×1) superstructure on the (110) surface (see Fig. 4). The formation of these ordered phases on the surface is easier than in the bulk, due to the higher mobility of the atoms on the surface. The calculations for the $L1_2$ phase showed that expansion of the surface yields stronger Ni enrichment of the surface layer and will, therefore, not be presented here. However, for the $L1_0$ phase the situation is different. The $L1_0$ ordering takes place at a compositional range of approximately 50% Pt. Due to preferential sputtering of Ni during sample preparation, the surface layers are Pt enriched up to $\approx 40\%$ (mean value of the two topmost layer compositions in Refs. 4,5). Further Pt enrichment is caused by segregation into the expanded areas due to the size effect.²⁰ This makes it possible for the $L1_0$ ordering to develop, which is also suggested by the composition of the first two layers shown in Fig. 1. Chemical ordering, due to the $L1_0$ phase, has already been observed in the Pt enriched surface layers of a $\text{Pt}_{25}\text{Ni}_{75}$ (111) sample.⁶

With a perfectly $L1_0$ ordered slab crystal, there are three different possibilities for the (110) surface as shown in Fig. 4: (i) pure Ni on the surface, (ii) pure Pt on the surface, and (iii) alternating Pt and Ni chains oriented in the $[\bar{1}10]$ direction on the surface. The latter matches perfectly with the observed corrugation pattern near the dislocation cores, whereas the first could represent the situation in the undisturbed regions.

We have constructed slab crystals for each of these three possible configurations and calculated the total energy in dependence of the expansion or compression in the two surface directions. The slabs consisted of 23 layers, which is equivalent to a thickness of the strained region of approximately 11 layers per surface. Because the three slabs did not consist of

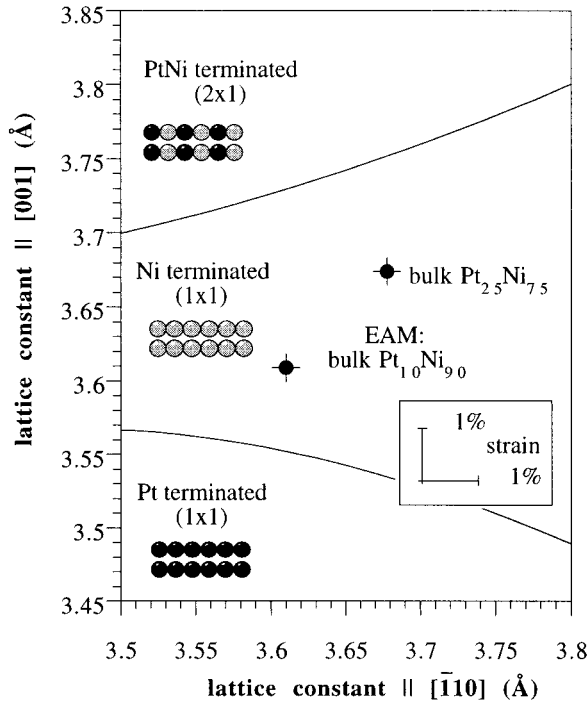


FIG. 5. Phase diagram for the differently terminated $L1_0$ slabs in dependence of the lattice constants in $[\bar{1}10]$ and $[001]$ direction for $T=0$ K obtained by embedded-atom method energy minimization calculations ($\Delta\mu_{\text{PtNi}}=1.5$ eV). The bulk lattice constants for $\text{Pt}_{10}\text{Ni}_{90}$ and $\text{Pt}_{25}\text{Ni}_{75}$ (from EAM Monte Carlo calculations) represent the unstrained surface. The bars indicate 1% strain in $[\bar{1}10]$ and $[001]$ direction. All lattice constants in Å.

the same number of Pt atoms, it is not possible to compare their energies directly. Instead, one has to subtract the difference in chemical potentials from the energy, i.e., the values of $E_{\text{tot}} - \Sigma\Delta\mu$ must be compared. With bulk Monte Carlo calculations (periodic boundary conditions in all three directions), we have determined the chemical potential difference $\Delta\mu$ between one Pt and one Ni atom to be in the range of 1.2 eV to 1.6 eV for the $L1_0$ phase at $T=500$ K.

For each surface configuration, the calculated energy values for different lattice constants have been fitted by a two dimensional second order polynomial. By intersecting these curves — and taking into account the difference in chemical potentials as a parameter — it is possible to create a phase diagram showing which configuration is energetically favored at temperature $T=0$ K. This phase diagram is shown in Fig. 5.

The filled circles indicate the $\text{Pt}_{10}\text{Ni}_{90}$ and $\text{Pt}_{25}\text{Ni}_{75}$ bulk lattice constants and, therefore, represent the unstrained surface. It can be seen that these points lie in the section of the phase diagram where Ni on the surface is energetically favored. The energetic difference, i.e., the difference in $E_{\text{tot}} - \Sigma\Delta\mu$, between the unstrained Ni-terminated and Pt-terminated slabs, is in the order of 50–100 meV per surface atom of the 23 layer slabs whereas the difference between the Ni-terminated and the PtNi-terminated slabs is in the order of 200–250 meV per surface atom.

If the slab is expanded along the close packed rows in the $[\bar{1}10]$ direction, the Ni-terminated surface stays energetically

stable. However, if the slab is expanded perpendicular to the close packed rows in the $[001]$ direction, the energetic difference between the Ni-terminated and the PtNi-terminated slab becomes smaller and vanishes at the expansion indicated by the phase separation line. With further expansion in the $[001]$ direction, the surface with 50% Pt and 50% Ni becomes the stable one. It has to be mentioned that the phase separation line between the Ni-terminated and the PtNi-terminated configuration is almost independent of the value of $\Delta\mu$, whereas the curve between the Ni-terminated and the Pt-terminated surfaces, strongly depends on $\Delta\mu$. The value chosen for $\Delta\mu$ agrees with the fact that for the unstrained surface, the Ni termination is the stable one.

As mentioned in Sec. II B, the experimentally observed expansions are $\approx 5\%$ in $[\bar{1}10]$ direction and 1%–2% in $[001]$ direction. In the simulation, a higher expansion in $[001]$ direction is necessary to get into the region where the PtNi surface [and, therefore, the (2×1) superstructure] is energetically favored. However, this could be due to the overestimated tetragonal distortion in the EAM simulations, as will be explained later.

We have also performed Monte Carlo simulations at $T=500$ K with differently expanded slab configurations in order to check for an influence of temperature on the ordering process. Without expansion the surface consisted of mainly Ni, whereas an expansion in the $[001]$ direction of approximately 4% yielded the observed (2×1) ordering.

We have further checked the average height of the Pt and Ni atoms in the computer simulation of the ordered phase to see if the corrugation pattern could be caused by atoms sitting in different heights. Whereas the measured corrugation difference is about 10–20 pm, the difference in height in the computer simulations is in the order of only 1 pm. Furthermore, the atom type sitting in the higher position was not the same in different simulation runs. This leads to the conclusion that the observed (2×1) corrugation pattern is due to chemical resolution caused by different electronic structure or different tip-sample interaction of Pt and Ni atoms.

C. Calculations with elasticity theory

To further verify the above explanation for the corrugation pattern, we used a completely independent method for calculating the energies of the $L1_0$ ordered slabs based on linear elasticity theory. For using the elasticity theory, the elastic constants have to be known. Although there are values for the elastic constants for pure Pt and pure Ni in literature, we did not find any experimental values for the ordered $L1_0$ phase. Therefore, we calculated the bulk elastic constants for the PtNi $L1_0$ phase with effective medium theory (EMT).^{21–23}

For the slabs, however, the boundary conditions for the stress components are different from the bulk. Because there are no forces acting on the free surfaces of the slab the stress components perpendicular to the surface vanish. Taking this into account, we have transformed the elastic constants to a coordinate system, where two coordinates lie in the surface plane and the third is perpendicular to the surface. Assuming no in-plane shear, we obtained the following expression for the elastic energy of a slab,

TABLE IV. Bulk elastic constants c_{ij} for Pt, Ni, and the tetragonal PtNi $L1_0$ phase and stress/strain ratios C_{ij} for the differently terminated $L1_0$ ordered PtNi slabs with free surfaces calculated with EMT in GPa.

	c_{11}	c_{12}	c_{13}	c_{33}	c_{44}	c_{66}
Pt	365	285			98	
PtNi $L1_0$	325	148	200	183	134	55
Ni	246	151			146	
	C_{11}	C_{12}	C_{21}	C_{22}	C_{66}	
100% term.	190	80	80	48	133	
50%/50% term.	326	162	162	141	80	

$$w = \frac{1}{2} [C_{11}\epsilon_1'^2 + 2C_{12}\epsilon_1'\epsilon_2' + C_{22}\epsilon_2'^2], \quad (4)$$

where ϵ_i' is the strain in direction i in the surface and the C_{ij} are constants describing the stress/strain ratios for a slab with free surfaces. Table IV lists the values for the bulk elastic constants together with the C_{ij} .

With respect to the elastic energy, there are two different (110) surfaces: (i) pure Ni or pure Pt on the surface (energetically equal), and (ii) 50% Pt and 50% Ni on the surface. This means that the last two slab types in Fig. 4 have the same elastic energy while for the PtNi-terminated slab due to the tetragonal distortion, the energy is different.

We have calculated the elastic energies for the two types of slabs with Eq. (4) in dependence of the strain in the two surface directions. By intersecting these two energy surfaces, we obtained the phase diagram for $T=0$ K shown in Fig. 6.

As can easily be seen, the unstrained slabs (represented by the $\text{Pt}_{10}\text{Ni}_{90}$ and $\text{Pt}_{25}\text{Ni}_{75}$ bulk lattice constants) are in the region where the pure surface (100% Ni) is energetically favored. If the slab is strained in the $[\bar{1}10]$ direction (along the close packed rows), the 100%-terminated slab is still the stable configuration. However, if the slab is expanded in the $[001]$ direction, the slab with the PtNi surface has the lower energy. This behavior is quite similar to the results of the EAM simulations. In contrast to the EAM phase diagram, the phase separation line has a negative slope. Thus, an expansion in the $[\bar{1}10]$ direction reduces the necessary strain in the $[001]$ direction for the PtNi surface to become energetically favored.

IV. DISCUSSION

Several theoretical predictions^{11,12} indicate that there is a metastable phase for the PtNi (110) surface, which could—under special experimental conditions—lead to segregation reversal with an oscillating segregation profile similar to the stable phase, but with Pt enrichment in the first layer and Pt depletion in the second. This would be the case if the $L1_2$ ordering was the reason for the (2×1) superstructure, as there would be a change in segregation from Ni (0% Pt) to PtNi (50% Pt) enrichment on the surface with respect to the average concentration (25% Pt). However, our EAM calculations have shown that, for the $L1_2$ ordered slab, the Ni-terminated surface is energetically favored in expanded re-

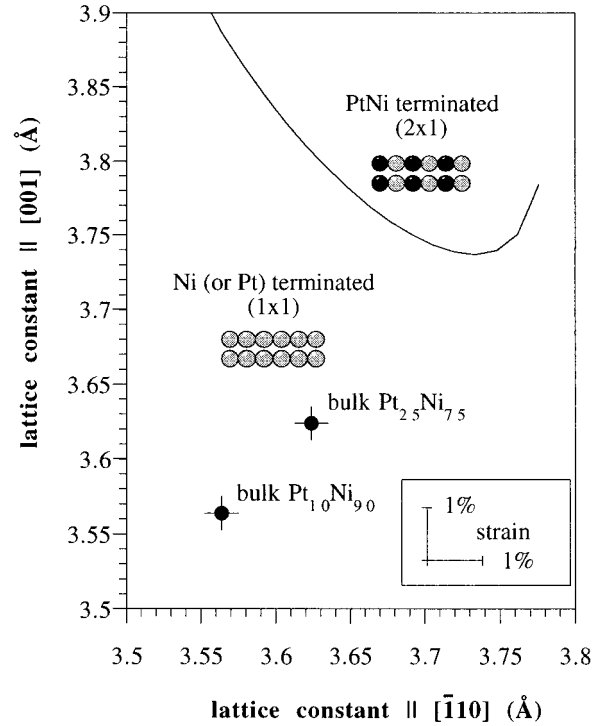


FIG. 6. Phase diagram for the differently terminated $L1_0$ slabs in dependence of the lattice constants in $[\bar{1}10]$ and $[001]$ directions for $T=0$ K derived from the elastic energy. The bulk lattice constants for $\text{Pt}_{10}\text{Ni}_{90}$ and $\text{Pt}_{25}\text{Ni}_{75}$ (calculated with Vegard's rule) represent the unstrained surface. The bars indicate 1% strain in the $[\bar{1}10]$ and $[001]$ direction.

gions (independent of the direction of expansion). A simple explanation for this behavior can be deduced from the elastic properties of the surface. On the open (110) surface, the atoms in the first layer are only weakly bound to each other. Thus, the surface layer is elastically soft with respect to the layers below and can be strained more easily.²⁰ If the slab is expanded, it can alleviate stress by moving the larger Pt atoms from the soft surface to the deeper harder layers, which partly compensates the strain. Therefore, the Ni-terminated surface has the lower energy.

For the $L1_0$ ordering, the phase diagrams show that, in regions expanded in the $[001]$ direction, there is a change in segregation behavior. But it is no segregation reversal as proposed in Refs. 11,12, because the surface composition changes from Ni enrichment to no segregation at all (50% Pt in all layers).

Based on the simulation calculations, we can explain the driving force for the locally altered chemical ordering in the strained region near the dislocation cores. The cause for the sensitivity to strain is the tetragonal distortion of the ordered $L1_0$ phase. Because the $L1_0$ structure is not cubic, the two kinds of (110) surfaces mentioned above have different geometry, as is shown in Fig. 7. The surface with 100% Ni [Fig. 7(b)] has a smaller distance between the $[\bar{1}10]$ oriented close packed rows than the PtNi surface [Fig. 7(c)], whereas the distance between the atoms in the close packed rows is

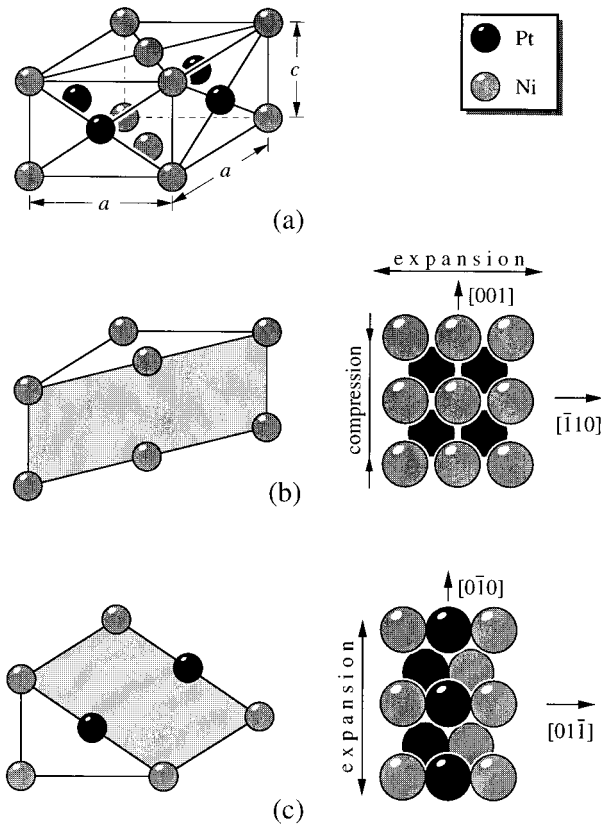


FIG. 7. The ordered $L1_0$ $\{110\}$ surfaces (tetragonal distortion strongly exaggerated). (a) $L1_0$ bulk structure. (b) Ni terminated $\{110\}$ truncated bulk and top view of the $\{110\}$ surface. The surface is expanded in the $[\bar{1}10]$ direction and compressed in the $[001]$ direction with respect to the cubic bulk. (c) PtNi terminated $\{110\}$ truncated bulk. The surface is expanded in the $[001]$ direction and has an almost unchanged lattice constant in the $[\bar{1}10]$ direction with respect to the cubic bulk.

smaller on the PtNi surface with respect to the pure Ni surface. To alleviate stress, the atoms in a region strained in the $[001]$ direction arrange in such a way that the “natural” distance between the close packed rows is higher. That is the case with the PtNi surface, which gives the observed (2×1) superstructure. In unstrained regions or in regions expanded only in the $[\bar{1}10]$ direction, the distance between the close packed rows is smaller. Therefore, the pure Ni surface has to be less distorted and gives lower stress.

We have found qualitative agreement between experiment and the computed phase diagrams. Both indicate that an expansion in $[001]$ direction is necessary for the (2×1) ordering to occur. However, the expansion needed in the calculations is approximately two times higher than what we have found experimentally. This quantitative difference could be caused by several reasons. The simulation does not account for the fact that the surface is not only strained, but also bent, which leads to an inhomogeneous strain field. Furthermore, the embedded-atom potentials used overestimate the tetragonal distortion of the $L1_0$ phase. As explained above, this distortion is the driving force for the strain dependence of the surface composition. The larger the difference between a and

c is, the more expansion is needed for the PtNi surface to be energetically favored.

The ordering is only of short range, just like the $L1_0$ ordering on PtNi(111) (Ref. 6), as can be derived from the fact that there are antiphase boundaries visible in the ordered region (see Fig. 2). Another indication for a short range order is that we did not find double steps with the STM, as could be expected with a long range ordering to avoid pure Pt termination.

Whereas we have observed local chemical ordering in the strain field of dislocations at the surface, such a phenomenon may also exist in the bulk if the composition is in the range where the $L1_0$ structure can develop (or in other cases where chemical ordering distorts the elementary cell). Such dislocations would be immobilized, because unimpeded movement of the dislocations (and therefore of the strain field) would require a reorientation of the $L1_0$ structure in the differently oriented domains. In other words, annealing of such a crystal could cause the dislocation to become self-trapped by the local chemical order, which could raise the yield stress as is the case with dislocations (superlattice dislocations) in superlattice alloys.²⁴ However, in contrast to superlattice dislocations, no long range but only short range order is necessary for the dislocation to become self-trapped.

V. CONCLUSIONS

We have presented STM measurements of bulk dislocations and sputter-induced edge dislocations on $\text{Pt}_x\text{Ni}_{1-x}$ alloy single crystal (110) surfaces (with $x=0.1$ and $x=0.25$). The STM images showed a (2×1) corrugation superstructure in the vicinity of the dislocation cores, whereas, in unstrained regions, the atoms had the same apparent height. Determination of the atomic distances with image processing revealed that the (2×1) pattern occurs in regions, where the surface is expanded both in the $[\bar{1}10]$ and $[001]$ direction. The differently bright atoms in the (2×1) structure have been identified as Pt and Ni.

We have performed computer simulations with embedded-atom potentials to determine the nature and the origin of the observed (2×1) superstructure. We have checked out the ordered $L1_2$ and $L1_0$ phases, which are both possible due to Pt enrichment of the surface caused by sample preparation. As a simplified simulation model for the strained region, we used differently expanded slabs. It has been found that only the $L1_0$ phase could lead to the superstructure in the expanded regions. In particular, an expansion in $[001]$ direction is necessary in the simulation for the (2×1) pattern to occur.

We further have compared the EAM simulations to calculations based on linear elasticity theory. Although the phase diagram looks somewhat different, the conclusion that only an expansion in the $[001]$ direction leads to the (2×1) superstructure stays the same.

The measurements together with the simulation calculations show that, in the expanded regions near dislocation cores, the chemical ordering changes due to strain. The surface is enriched locally with Pt. This altered surface compo-

sition is not caused by a metastable state becoming energetically favored as previous theoretical predictions could indicate, but rather is due to a reorientation of the tetragonal ordered $L1_0$ structure in the strained region, which reduces the surface stress. Finally, we have pointed out that local chemical ordering in the strain field of dislocations might also occur in the bulk, which could immobilize the dislocations and, therefore, raise the yield stress of a material.

ACKNOWLEDGMENTS

We are very grateful to S.M. Foiles (Sandia National Laboratory, Livermore) for supplying us with the EAM computer code and to J.C. Bertolini, who has provided the $\text{Pt}_{10}\text{Ni}_{90}$ (110) crystal. This work was supported by the "Fonds zur Förderung der Wissenschaftlichen Forschung" (Austrian Science Foundation) under Projects Nos. S6201 and S6204.

- ¹Y. Gauthier and R. Baudoing, in *Surface Segregation Phenomena*, edited by P. A. Dowben and A. Miller (CRC Press, Boca Raton, FL, 1990), p. 169.
- ²P. Weigand, P. Novacek, G. van Husen, T. Neidhart, and P. Varga, *Surf. Sci.* **269/270**, 1129 (1991).
- ³P. Weigand, P. Novacek, E. Taglauer, G. van Husen, T. Neidhart, L. Z. Mezey, W. Hofer, and P. Varga, *Nucl. Instrum. Methods Phys. Res. Sect. B* **64**, 93 (1992).
- ⁴P. Weigand, B. Jelinek, W. Hofer, and P. Varga, *Surf. Sci.* **295**, 57 (1993).
- ⁵P. Weigand, B. Jelinek, W. Hofer, and P. Varga, *Surf. Sci.* **301**, 306 (1994).
- ⁶M. Schmid, H. Stadler, and P. Varga, *Phys. Rev. Lett.* **70**, 1441 (1993).
- ⁷M. Schmid, A. Biedermann, H. Stadler, C. Slama, and P. Varga, *Appl. Phys. A* **55**, 468 (1992).
- ⁸M. Schmid, A. Biedermann, H. Stadler, and P. Varga, *Phys. Rev. Lett.* **69**, 925 (1992).
- ⁹M. Schmid, A. Biedermann, C. Slama, H. Stadler, P. Weigand, and P. Varga, *Nucl. Instrum. Methods Phys. Res. Sect. B* **82**, 259 (1993).
- ¹⁰P. Weigand, W. Hofer, and P. Varga, *Surf. Sci.* **287/288**, 350 (1993).
- ¹¹M. Lundberg, *Phys. Rev. B* **36**, 4692 (1987).
- ¹²B. Legrand, G. Tréglia, and F. Ducastelle, *Phys. Rev. B* **41**, 4422 (1990).
- ¹³Y. Gauthier, R. Baudoing, and J. Jupille, *Phys. Rev. B* **40**, 1500 (1989).
- ¹⁴S. D. Böhmig, M. Schmid, and H. Störi, *Surf. Sci.* **313**, 6 (1994); *Fresenius J. Anal. Chem.* **353**, 439 (1995).
- ¹⁵M. S. Daw and M. I. Baskes, *Phys. Rev. B* **29**, 6443 (1984).
- ¹⁶A. F. Voter, S. P. Chen, R. C. Albert, A. M. Boring, and P. J. Hay, in *Atomistic Simulation of Materials — Beyond Pair Potentials*, edited by V. Vitek and D. J. Srolovitz (Plenum, New York, 1989), p. 223.
- ¹⁷J. H. Rose, J. R. Smith, F. Guinea, and J. Ferrante, *Phys. Rev. B* **29**, 2963 (1984).
- ¹⁸H. Stadler, W. Hofer, M. Schmid, and P. Varga, *Surf. Sci.* **287/288**, 366 (1993).
- ¹⁹S. M. Foiles, M. I. Baskes, and M. S. Daw, *Phys. Rev. B* **33**, 7983 (1986).
- ²⁰M. Schmid, W. Hofer, P. Varga, P. Stolze, K. W. Jacobsen, and J. K. Nørskov, *Phys. Rev. B* **51**, 10 937 (1995).
- ²¹K. W. Jacobsen, J. K. Nørskov, and M. J. Puska, *Phys. Rev. B* **35**, 7423 (1987).
- ²²K. W. Jacobsen, *Comments Condens. Matter. Phys.* **14**, 129 (1988).
- ²³P. Stoltze, *J. Phys. Condens. Matter* **6**, 9495 (1994).
- ²⁴N. S. Stoloff, in *Strengthening Methods in Crystals*, edited by A. Kelly and R. B. Nicholson (Elsevier, London, 1971), p. 193.
- ²⁵C. Amador, W. R. L. Lambrecht, and B. Segall, *Phys. Rev. B* **47**, 15 276 (1993).
- ²⁶W. Hofer, *Fresenius J. Anal. Chem.* **346**, 246 (1993).